Low-Frequency Stability Analysis of Vehicle-Grid System With Active Power Filter Based on *dq*-Frame Impedance

Siqi Wu, *Student Member, IEEE*, and Zhigang Liu, *Senior Member, IEEE*

***Abstract*—To eliminate the low-frequency oscillation (LFO) phenomenon in the vehicle-grid system of high-speed railways, a single-phase cascaded H-bridge multilevel active power filter (APF) directly accessed to the 27.5-kV traction network is proposed in this article, which can provide the dynamic reactive and interharmonic compensation. To explore the mechanism of APF on LFO suppression, the *dq*-frame impedance model of vehicle-grid system with APF is established first. The impact of the second-order generalized integrator model and the duty ratio model on the impedance accuracy is discussed in detail. Then, based on the generalized Nyquist stability criterion and system power consumption criterion, the stability of vehicle-grid system and its sensitivity to parameters in different cases are compared. The results indicate that the proposed APF can significantly improve the low-frequency stability of vehicle-grid system and owns much better performance than the STATCOM proposed in previous literatures. Finally, the time-domain simulations in MATLAB and the experiments on the controller hardware in the loop platform are implemented, which further validate the accuracy of theoretical analysis and the superior performance of APF in LFO elimination.**

***Index Terms*—Active power filter (APF), impedance, low-frequency oscillation (LFO), stability margin, vehicle-grid system.**

I. Introduction

NOWADAYS, high-speed railways develop rapidly in China and even all over the word. The ac–dc–ac drive electric multiple units (EMUs) and electric locomotives (hereafter called vehicles) are accessed to the traction power grid (hereafter called grid) at high density. In consequence, the vehicle-grid system becomes a typical single-phase power electronics-based system. The interactions between the vehicles and grid have resulted in some instability phenomena worldwide, such as the harmonic instability, the low-frequency oscillation (LFO), and the harmonic resonance [1]–[2]. Among them, the LFO usually happens when multiple vehicles are at standstill in a railway depot with only the auxiliary load energized, as shown in Fig. 1, in which the grid current, grid voltage, and dc-side voltage of the rectifier all oscillate at a low frequency. Since the traction motors are not working in this situation, the dc-side load of the rectifier is usually simplified to a pure resistor. The high voltage peak could easily trigger the system protection logic devices and lead to traction blockade of vehicles, which threatens the normal operation of vehicle-grid system [3]. At present, some research has been implemented to explore the mechanism of LFO. It is well accepted that the LFO, which occurs easily under a weak grid, mainly results from the mismatching between the grid impedance and vehicles impedance [4].

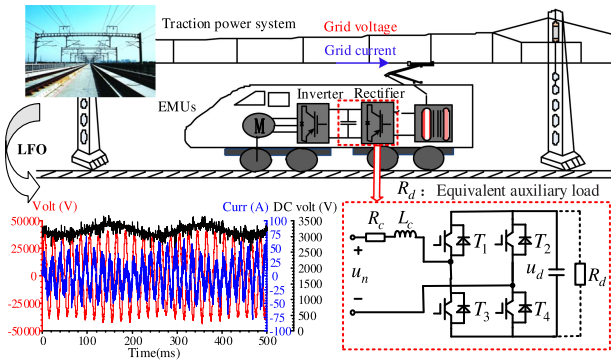

Fig. 1. LFO in vehicle-grid coupling system.

In fact, the LFO can be regarded as a dynamic stability issue of large-scale multiconverter system under certain conditions. For the impedance-based stability analysis, the vehicle-grid system is usually decomposed into two cascaded subsystems, namely the grid as the source subsystem and the vehicles as the load subsystem. Based on the impedance ratio of the source and load, the stability of the whole system can be determined. Therefore, the LFO mitigation methods are able to fall into two categories for source impedance reshaping or load impedance reshaping. Specifically, in terms of load impedance reshaping, several measures have been proposed, which mainly focus on the optimization of the internal structure of vehicles, such as tuning the control parameters and improving the control strategies [5]–[7]. Moreover, aiming at the reactive current generated by the vehicles in abnormal states as LFO occurs, a single-phase cascaded H-bridge multilevel static synchronous compensator

Manuscript received April 24, 2020; revised July 11, 2020 and October 7, 2020; accepted December 30, 2020. Date of publication January 5, 2021; date of current version May 5, 2021. This work was supported in part by the National Nature Science Foundation of China under Grant U1734202, in part by the Research Project of China Railway Eryuan Engineering Group Co., Ltd., under Grant KYY2020033(20-21), and in part by the National Key R&D Program of China under Grant 2016YFB1200601-A01. Recommended for publication by Associate Editor R. Burgos. *(Corresponding author: Zhigang Liu.)*

The authors are with the School of Electrical Engineering, Southwest Jiaotong University, Chengdu 611756, China (e-mail: wusq_jtu@163.com; liuzg_cd@126.com).

Color versions of one or more figures in this article are available at https://doi.org/10.1109/TPEL.2021.3049145.

Digital Object Identifier 10.1109/TPEL.2021.3049145

(STATCOM) was proposed in [8], which can be directly accessed to the grid for reactive compensation to restrain the LFO. Different from the measures in [5]–[7], the STATCOM actually works as a power regulator, which can be applied under various conditions and reshape the load impedance without any change on the rest parts of the system. However, although the low-frequency stability of the vehicle-grid system is enhanced effectively with STATCOM, it is still sensitive to the parameters of vehicles, with which the system stability margin varies significantly.

When LFO occurs, the grid voltage or current is modulated by a signal in low frequency, which indicates that, except the reactive current, there are also a large amount of interharmonic currents generated in the grid [9]. In [10], the active power filter (APF) was established to deal with the emerging power quality problems of high-speed railways and obtained a fine compensation effect. In recent years, multilevel converters have become more and more popular in high power applications, which can be directly hooked up to the grid without any step-down transformer. In this article, a cascaded H-bridge (CHB) multilevel APF is designed to restrain the LFO occurring when multiple China Railway High-speed 5 (CRH5) EMUs are accessed to the grid, which is able to solve the reactive power shortage problem as well as the interharmonic problem. In order to reveal the mechanism of APF on LFO suppression and assess the influence of APF on the stability of vehicle-grid system, the impedance-based stability analysis method with generalized Nyquist stability criterion (GNSC) and the system power consumption criterion are adopted [11]–[12]. At present, various impedance modeling techniques have been proposed [13]–[15], such as the *dq*-frame modeling technique, the harmonic state-space modeling technique, and the $\alpha\beta$-frame modeling technique, but none of them is utilized for APF in single-phase system. In this article, the active and reactive currents detection and grid-synchronization in APF proposed are both realized on *dq* frame, so the *dq*-frame impedance modeling method is selected. Since the current tracking controller of APF is implemented on the $\alpha\beta$ frame, it needs to be equivalently transformed to the *dq* frame first. Compared with the rectifier in [16] whose current controller is directly conducted on the *dq* frame, the APF proposed is different in both the main circuit topology and the control structure, which leads to the difference in their modeling processes in *dq* frame. In the following, the main contributions of this article are summarized.

1) Through equivalence, the current tracking controller of APF is transformed to *dq* frame, and the closed-loop input impedance of the vehicle-grid system with APF in *dq* frame is deduced in detail for further stability analysis.
2) The influence of the second-order generalized integrator (SOGI) model and the duty ratio model on the *dq*-frame impedance accuracy of the whole system is revealed, which fills a gap in existing articles.
3) Based on the GNSC and system power consumption criterion, the mechanism of APF on LFO suppression and the influence of two different compensation modes on the stability of vehicle-grid system are elucidated. Besides, the system parameters sensitivity under different conditions is compared and discussed.
4) The superior performance of APF in LFO elimination is validated by the simulations in MATLAB and experiments on the controller hardware in the loop (HIL) platform.

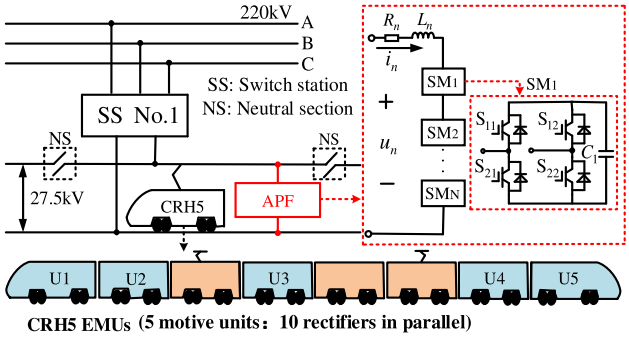

Fig. 2. Circuit configuration of the APF for the vehicle-grid system.

The rest of this article is organized as follows. In Section II, the circuit configuration and operating principle of APF are illustrated. In Section III, the closed-loop input impedance of vehicle-grid system with APF in *dq* frame is deduced in detail. In Section IV, the verification of the analytical impedance model is presented and the influence factors of the impedance accuracy are revealed. In Section V, the stability analysis is implemented in multiple situations to explore the operation mechanism and effect of APF. In Sections VI and VII, the suppression effect of APF on the LFO is verified via the simulations in MATLAB and experiments on the controller HIL platform, respectively. Finally, Section VIII concludes the article.

II. Design of the Cascaded H-Bridge Multilevel APF

The circuit configuration of the vehicle-grid system with APF is depicted in Fig. 2, where the APF is directly accessed to the 27.5-kV traction power grid. u_n denotes the grid voltage and i_n denotes the input current of APF. The *N* submodules (SMs) of the cascaded H-bridge converter are connected in series and the dc-side capacitors of SMs own the same voltage reference. U1, U2, …, U5 present the motive units in CRH5 EMUs, each of which contains two rectifiers in parallel with the identical structure. Namely, one CRH5 EMUs contains ten rectifiers. Fig. 3 describes the control structure of APF, which mainly consists of the dc voltage controller, the interharmonic and reactive current detector and the current tracking controller. i_s denotes the grid current and i_c denotes the input current of vehicles. For a single-phase system, there is only one phase and two orthogonal signals do not exist. This is different from the three-phase systems where the α-axis and β-axis components can be created directly via the Clarke transform from phase quantities *abc* to $\alpha\beta$. Hence, to realize the control in *dq* frame, two SOGIs are selected here as the orthogonal signal generators, which can construct the 90° phase shifted versions of the original variables, namely the virtual β-axis components, for Park transform [17]. The control structure of SOGI will be presented in Section III. Here, the grid synchronization is realized via the SOGI-based phase-locked-loop (PLL). It is noted that the APF can operate

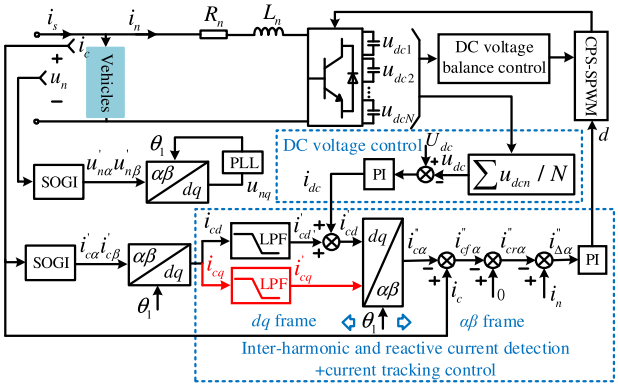

Fig. 3. Control structure of the CHB multilevel APF.

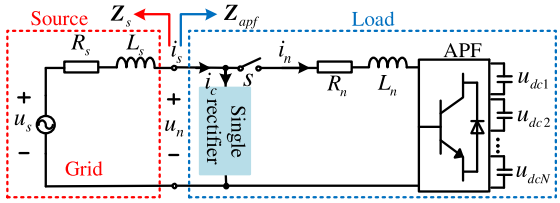

Fig. 4. Simplified vehicle-grid system with APF.

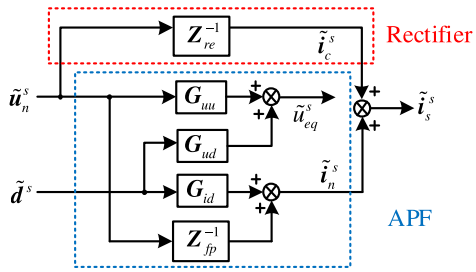

Fig. 5. Open-loop small signal model of single-phase rectifier system with APF in *dq* frame.

in two different modes. In Mode 1, APF is only applied for interharmonic compensation, while in Mode 2, APF is applied for interharmonic and reactive compensation. Fig. 3 describes the control strategy for Mode 1. Through Park transform, the fundamental active current and reactive current absorbed by the vehicles become the dc terms in *d*-axis and *q*-axis, respectively, while the interharmonics are converted to ac quantities with fundamental frequency shift. So the dc components ($i'_{cd'}$ and i'_{cq}) can be extracted via the low-pass filters (LPFs). Subtracting the inverse Park transform results of $i'_{cd'}$ and i'_{cq} from the input current of vehicles i_c, the interharmonic components in i_c are then detected. In this regard, if the reactive compensation is further required, the control structure drawn in red lines should be removed, so the *q*-axis input current of inverse park transform is equal to zero and the detected current $i''_{cf\alpha}$ will contain both the reactive and interharmonic components in i_c. By inverting $i''_{cf\alpha}$, the input current reference of APF is obtained. Moreover, as shown in Fig. 3, a dc voltage controller is added in the *d* channel, which is utilized to control the active power exchange between the grid and APF as the dc-side voltage fluctuates.

In general, for this article, APF is controlled under two different operation modes, so as to explore the effects of different compensation methods on LFO inhibition. The low-frequency stability of vehicle-grid system when APF operates in Mode 1 and Mode 2 is comprehensively compared.

III. D-Q Frame Impedance Modeling

To realize the impedance-based stability analysis, the *dq*-frame impedance model of vehicle-grid system with CHB multilevel APF is developed in this section. As mentioned in Section I, the vehicle-grid system usually enters into a low-frequency unstable state when multiple vehicles are hooked up to the grid. In this regard, there are tens or hundreds of rectifiers in operation. The whole system is really complex, which can significantly reduce the efficiency of impedance measurement and simulation verification. Thus, the vehicle-grid system is equivalent to the model in Fig. 4, where a single-phase rectifier is connected to the grid with a large inductance L_s. u_s represents an ideal voltage source. $\boldsymbol{Z}_s$ and $\boldsymbol{Z}_{apf}$ denote the *dq*-frame impedances of grid and rectifier system with APF, respectively. In the following, the modeling process of $\boldsymbol{Z}_{apf}$ considering the main circuit and all controllers is illustrated in detail.

A. Main Circuit of APF

Since the switching frequency of APF is high, the dc-side voltages of submodules can be regarded as the same without deviation [18]. In the impedance model, the CHB converter in Fig. 4 is equivalent to a two-level converter with the dc-side voltage u_{eq} and capacitance C_{eq} in

$$u_{eq} = \sum_{n=1}^{N} u_{dcn} = N u_{dc}; C_{eq} = \frac{C_n}{N}. \tag{1}$$

For the vehicle-grid system, there is only one phase. If the original grid voltage u_n, input current of APF i_n, and duty ratio *d* are regarded as the α-axis components, there will be no actual components in β-axis (i.e., β-axis system). Hence, to establish the *dq*-frame model, the virtual β-axis components are defined as the signals that lag the actual α-axis components by 90° while maintaining the amplitudes, e.g., $u_{n\beta}(s) = -ju_{n\alpha}(s) = -ju_n(s)$. Then, the Park transform and its inverse can make sense. Here, through the latter, we can obtain the following, where *v* denotes the related variable and ω denotes the fundamental angular frequency

$$v(t) = v_\alpha(t) = v_d(t)\sin\omega t + v_q(t)\cos\omega t. \tag{2}$$

For clarity, the superscript *s* of each signal represents the system *dq* frame, which will be introduced in the following analysis. U^s_{nd}, U^s_{nq}, I^s_{nd}, I^s_{nq}, D^s_d, D^s_q, and U_{eq} are defined as the dc steady-state values at a fixed point. "~" represents the small-signal perturbation of a signal. Based on (2), the main circuit of APF and the linearization around the steady-state operating points, the transfer function matrix flow plot shown in the blue dotted frame in Fig. 5 can be derived. The red dotted frame part depicts the closed-loop small signal model of the rectifier system in *dq* frame. $\tilde{\boldsymbol{i}}^s_s = [\tilde{i}^s_{sd}\ \tilde{i}^s_{sq}]^{\mathrm{T}}$, $\tilde{\boldsymbol{i}}^s_n = [\tilde{i}^s_{nd}\ \tilde{i}^s_{nq}]^{\mathrm{T}}$,

$\tilde{\boldsymbol{i}}_c^s = [\,\tilde{i}_{cd}^s\ \tilde{i}_{cq}^s\,]^{\mathrm{T}}$, $\tilde{\boldsymbol{u}}_n^s = [\,\tilde{u}_{nd}^s\ \tilde{u}_{nq}^s\,]^{\mathrm{T}}$, and $\tilde{\boldsymbol{d}}^s = [\,\tilde{d}_d^s\ \tilde{d}_q^s\,]^{\mathrm{T}}$ are the space vector forms of variables. The expressions of the transfer function matrices $\boldsymbol{Z}_{fp}^{-1}$, $\boldsymbol{Z}_{re}^{-1}$, $\boldsymbol{G}_{uu}$, $\boldsymbol{G}_{ud}$, and $\boldsymbol{G}_{id}$ are presented in the Appendix.

B. Controller of APF

Because of the PLL, there exists two dq frames in APF. The system and control dq frames are defined via the voltage at the point of common coupling (PCC) u_n and the PLL, respectively. The phase deviation $\Delta\theta$ between these two dq frames will be generated when the system is perturbed [19]. So the park transform matrix $\boldsymbol{T}_{\theta l}$ can be presented as the product of matrix $\boldsymbol{T}_{\Delta\theta}$ and $\boldsymbol{T}_{\theta}$, as

$$\begin{aligned}\boldsymbol{T}_{\theta l} &= \begin{bmatrix}\cos(\theta_1-90^o) & \sin(\theta_1-90^o)\\ -\sin(\theta_1-90^o) & \cos(\theta_1-90^o)\end{bmatrix}\\ &= \begin{bmatrix}\cos(\theta-90^o) & \sin(\theta-90^o)\\ -\sin(\theta-90^o) & \cos(\theta-90^o)\end{bmatrix}\begin{bmatrix}\cos\Delta\theta & \sin\Delta\theta\\ -\sin\Delta\theta & \cos\Delta\theta\end{bmatrix}\\ &= \boldsymbol{T}_{\theta}\boldsymbol{T}_{\Delta\theta} = \boldsymbol{T}_{\Delta\theta}\boldsymbol{T}_{\theta}.\end{aligned} \tag{3}$$

where θ denotes the real phase of u_n. θ_1 denotes the locked phase output by PLL. As can be seen from Fig. 3, one part of the current controller is implemented on the dq frame, while the other part on the $\alpha\beta$ frame. Therefore, to constitute the dq-frame impedance, the latter need to be transformed to dq frame first. Here, the duty ratio vector $\boldsymbol{d}^s = [\,d_\alpha^s\ d_\beta^s\,]^{\mathrm{T}}$ in time domain can be expressed as

$$\begin{aligned}\begin{bmatrix}d_\alpha^s\\ d_\beta^s\end{bmatrix} &= -H_{PI}(t) * \left(\boldsymbol{T}_{\theta l}^{-1}\cdot\begin{bmatrix}i_{cd}^{c'}\\ i_{cq}^{c'}\end{bmatrix} - \begin{bmatrix}i_{c\alpha}^s\\ i_{c\beta}^s\end{bmatrix} - \begin{bmatrix}i_{n\alpha}^s\\ i_{n\beta}^s\end{bmatrix}\right)\\ &= -H_{PI}(t) * \left(\boldsymbol{T}_{\theta}^{-1}\cdot\boldsymbol{T}_{\Delta\theta}^{-1}\cdot\begin{bmatrix}i_{cd}^{c'}\\ i_{cq}^{c'}\end{bmatrix} - \boldsymbol{T}_{\theta}^{-1}\begin{bmatrix}i_{cd}^s\\ i_{cq}^s\end{bmatrix} - \boldsymbol{T}_{\theta}^{-1}\begin{bmatrix}i_{nd}^s\\ i_{nq}^s\end{bmatrix}\right)\end{aligned} \tag{4}$$

where

$$H_{PI}(t) = L^{-1}[H_{PI}(s)] = L^{-1}\left[k_{Pi} + \frac{k_{Ii}}{s}\right]. \tag{5}$$

in which k_{Pi} and k_{Ii} denote the proportional and integral gain of the PI controller in current inner-loop, respectively.

Ignoring the influence of k_{Ii} in (4), we can obtain

$$\begin{aligned}\begin{bmatrix}d_\alpha^s\\ d_\beta^s\end{bmatrix} \approx -\boldsymbol{T}_{\theta}^{-1}\cdot\Bigg\{k_{Pi}\cdot\Bigg(\boldsymbol{T}_{\Delta\theta}^{-1}\cdot\begin{bmatrix}i_{cd}^{c'}\\ i_{cq}^{c'}\end{bmatrix} - \boldsymbol{T}_{\theta}\begin{bmatrix}i_{c\alpha}^s\\ i_{c\beta}^s\end{bmatrix}\\ -\boldsymbol{T}_{\theta}\begin{bmatrix}i_{n\alpha}^s\\ i_{n\beta}^s\end{bmatrix}\Bigg)\Bigg\}.\end{aligned} \tag{6}$$

Based on (6), the control structure of APF can be equivalent to Fig. 6.

Fig. 7 shows the control structure of voltage SOGI and its equivalent simplified model for modeling, where K_{uS} is the proportional gain. $\boldsymbol{H}_{u\alpha\beta}$ is defined as the transfer matrix for voltage SOGI in $\alpha\beta$ frame. According to the properties of convolution and Laplace transform, we can combine $\boldsymbol{H}_{u\alpha\beta}$ with $\boldsymbol{T}_{\theta}$ to derive the transfer matrix $\boldsymbol{H}_{udq}$ for voltage SOGI in dq frame. Since the current SOGI owns the identical structure to

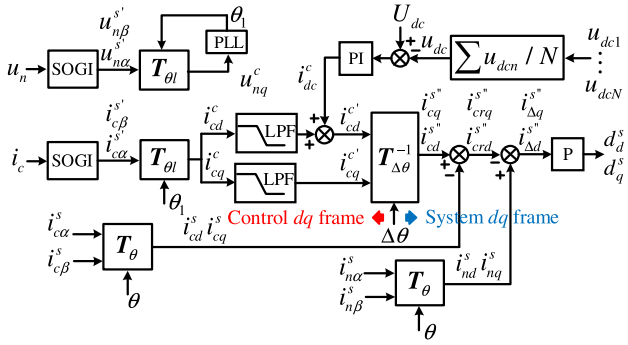

Fig. 6. Equivalent control of APF.

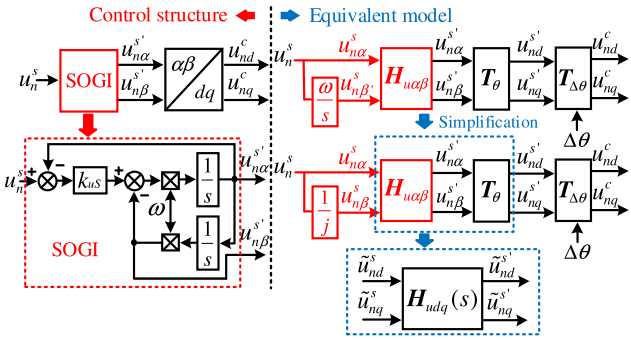

Fig. 7. Structure and equivalent model of voltage SOGI.

the voltage SOGI, the dq-frame transfer matrix for current SOGI can be deduced with the same approach.

From Fig. 6 and (3), the influences of PLL on $\tilde{\boldsymbol{i}}_c^c$ and $\tilde{\boldsymbol{i}}_c^{s''}$ can be evaluated and formulated as

$$\begin{aligned}\begin{bmatrix}\tilde{i}_{cd}^c\\ \tilde{i}_{cq}^c\end{bmatrix} &= \begin{bmatrix}0 & I_{cq}^{s'}G_{pll}\\ 0 & -I_{cd}^{s'}G_{pll}\end{bmatrix}\begin{bmatrix}\tilde{u}_{nd}^{s'}\\ \tilde{u}_{nq}^{s'}\end{bmatrix} + \begin{bmatrix}\tilde{i}_{cd}^{s'}\\ \tilde{i}_{cq}^{s'}\end{bmatrix}\\ &= \boldsymbol{G}_{pll}^{ic}\begin{bmatrix}\tilde{u}_{nd}^{s'}\\ \tilde{u}_{nq}^{s'}\end{bmatrix} + \begin{bmatrix}\tilde{i}_{cd}^{s'}\\ \tilde{i}_{cq}^{s'}\end{bmatrix}\end{aligned} \tag{7}$$

$$\begin{aligned}\begin{bmatrix}\tilde{i}_{cd}^{s''}\\ \tilde{i}_{cq}^{s''}\end{bmatrix} &= \begin{bmatrix}0 & -I_{cq}^{c'}G_{pll}\\ 0 & I_{cd}^{c'}G_{pll}\end{bmatrix}\begin{bmatrix}\tilde{u}_{nd}^{s'}\\ \tilde{u}_{nq}^{s'}\end{bmatrix} + \begin{bmatrix}\tilde{i}_{cd}^{c'}\\ \tilde{i}_{cq}^{c'}\end{bmatrix}\\ &= \boldsymbol{G}_{pll}^{icc}\begin{bmatrix}\tilde{u}_{nd}^{s'}\\ \tilde{u}_{nq}^{s'}\end{bmatrix} + \begin{bmatrix}\tilde{i}_{cd}^{c'}\\ \tilde{i}_{cq}^{c'}\end{bmatrix}\end{aligned} \tag{8}$$

where the expression of G_{pll} is presented in the Appendix. It is worth noticing that all the steady-state operating points with the superscripts s', s'', c, and c' are equal to those with superscript s except $I_{cd}^{c'}$, which is equal to I_{cd}^{c} plus I_{dc}^{c}. From Fig. 6, the transfer matrix $\boldsymbol{G}_{dc}$ of dc voltage controller can be obtained as

$$\boldsymbol{G}_{dc} = -\frac{1}{N}\begin{bmatrix}k_{Pu} + \frac{k_{Iu}}{s}\\ 0\end{bmatrix} \tag{9}$$

where k_{Iu} and k_{Pu} denote the integral and proportional gain of dc voltage controller, respectively, so the current $\tilde{\boldsymbol{i}}_c^{c'} = [\,\tilde{i}_{cd}^{c'}\ \tilde{i}_{cq}^{c'}\,]^{\mathrm{T}}$ can be derived as

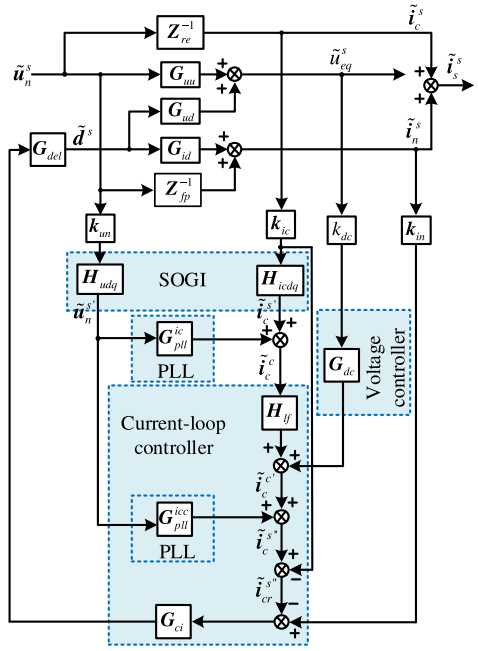

Fig. 8. Closed-loop small signal model of the rectifier system with APF.

$$\begin{bmatrix} \tilde{i}_{cd}^{c'} \\ \tilde{i}_{cq}^{c'} \end{bmatrix} = \boldsymbol{S}_{2x2} \begin{bmatrix} h_{lf1} & 0 \\ 0 & h_{lf2} \end{bmatrix} \begin{bmatrix} \tilde{i}_{cd}^{c} \\ \tilde{i}_{cq}^{c} \end{bmatrix} + \boldsymbol{G}_{dc} \cdot \tilde{u}_{eq} = \boldsymbol{H}_{lf} \begin{bmatrix} \tilde{i}_{cd}^{c} \\ \tilde{i}_{cq}^{c} \end{bmatrix} + \boldsymbol{G}_{dc} \cdot \tilde{u}_{eq} \tag{10}$$

where $\boldsymbol{S}_{2x2}$ reflects the operating mode of APF. When APF operates in Mode 1 and 2, $\boldsymbol{S}_{2x2}$ is equal to $\boldsymbol{A}_{2x2}$ and $\boldsymbol{B}_{2x2}$ in (11), respectively. In addition, h_{lf1} and h_{lf2} denote the transfer functions of LPFs, as shown in (12), in which ζ denotes the damping ratio. ω_{l1} and ω_{l2} denote the natural angular frequency of LPF in d channel and q channel, respectively

$$\boldsymbol{A}_{2x2} = \begin{bmatrix} 1 & 0 \\ 0 & 1 \end{bmatrix}, \boldsymbol{B}_{2x2} = \begin{bmatrix} 1 & 0 \\ 0 & 0 \end{bmatrix} \tag{11}$$

$$h_{lf1} = \frac{\omega_{l1}^2}{s^2 + 2\zeta\omega_{l1}s + \omega_{l1}^2}, h_{lf2} = \frac{\omega_{l2}^2}{s^2 + 2\zeta\omega_{l2}s + \omega_{l2}^2}. \tag{12}$$

Moreover, the duty ratio vector $\tilde{\boldsymbol{d}}^s$ can be derived as

$$\begin{bmatrix} \tilde{d}_d^s \\ \tilde{d}_q^s \end{bmatrix} = \begin{bmatrix} k_{Pi} & 0 \\ 0 & k_{Pi} \end{bmatrix} \begin{bmatrix} \tilde{i}_{\Delta d}^{s''} \\ \tilde{i}_{\Delta q}^{s''} \end{bmatrix} = \boldsymbol{G}_{ci} \left(\begin{bmatrix} \tilde{i}_{nd}^{s} \\ \tilde{i}_{nq}^{s} \end{bmatrix} - \begin{bmatrix} \tilde{i}_{crd}^{s''} \\ \tilde{i}_{crq}^{s''} \end{bmatrix} \right). \tag{13}$$

C. Closed-Loop Impedance of Rectifier System With APF

Fig. 8 shows the small-signal model of rectifier system with APF under closed-loop condition. The transfer matrices $\boldsymbol{k}_{un}$, $\boldsymbol{k}_{in}$, k_{dc}, and $\boldsymbol{k}_{ic}$ reflect the influence of signal sampling, while $\boldsymbol{G}_{del}$ reflects that of the time delay resulted from digital control and PWM. To simplify the modeling verification, these transfer matrices are not considered in this article. From Fig. 8, the impedance $\boldsymbol{Z}_{apf}$ of rectifier system with APF in closed-loop state

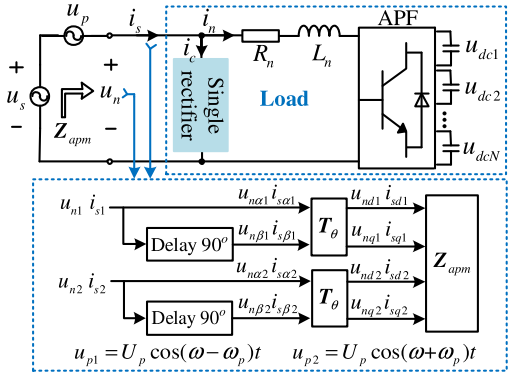

Fig. 9. Impedance measuring approach.

can be deduced as

$$\begin{aligned} \boldsymbol{Z}_{apf} = (((&\boldsymbol{G}_{id}(\boldsymbol{I}_{2x2} + \boldsymbol{G}_{del}\boldsymbol{G}_{ci}\boldsymbol{G}_{dc}k_{dc}\boldsymbol{G}_{ud})^{-1} \\ &\boldsymbol{G}_{del}\boldsymbol{G}_{ci}((\boldsymbol{k}_{ic} - \boldsymbol{H}_{lf}\boldsymbol{H}_{icdq}\boldsymbol{k}_{ic}) \\ &\cdot \boldsymbol{Z}_{re}^{-1} - (\boldsymbol{G}_{pll}^{icc} + \boldsymbol{H}_{lf}\boldsymbol{G}_{pll}^{ic})\boldsymbol{H}_{udq}\boldsymbol{k}_{un} - \boldsymbol{G}_{dc}k_{dc}\boldsymbol{G}_{uu}) \\ &+ \boldsymbol{Z}_{fp}^{-1})^{-1} \cdot (\boldsymbol{I}_{2x2} \\ &- \boldsymbol{G}_{id}(\boldsymbol{I}_{2x2} + \boldsymbol{G}_{del}\boldsymbol{G}_{ci}\boldsymbol{G}_{dc}k_{dc}\boldsymbol{G}_{ud})^{-1}\boldsymbol{G}_{del}\boldsymbol{G}_{ci}\boldsymbol{k}_{in}))^{-1} \\ &+ \boldsymbol{Z}_{re}^{-1})^{-1} \end{aligned} \tag{14}$$

where $\boldsymbol{I}_{2x2}$ denotes a 2-order identity matrix. $\boldsymbol{Z}_{apf}$ depicts the dynamics of the load subsystem, which can be combined with the grid impedance to achieve the system stability assessment.

IV. Impedance Verification and Discussion

In this section, the dq-frame impedance of rectifier system with CHB multilevel APF is measured, so as to validate the proposed modeling method in Section III. As shown in Fig. 9, two perturbations at frequency $\omega - \omega_p$ and $\omega + \omega_p$ are generated in the system by the voltage source u_p [16]. After the fabrication of virtual β-axis components and Park transform, the measured response voltages and currents in dq frame can be obtained. Then, the dq-frame impedance $\boldsymbol{Z}_{apm}$ at the perturbation frequency ω_p can be calculated as

$$\boldsymbol{Z}_{apm} = \begin{bmatrix} Z_{Ldd} & Z_{Ldq} \\ Z_{Lqd} & Z_{Lqq} \end{bmatrix} = \begin{bmatrix} \tilde{u}_{nd1} & \tilde{u}_{nd2} \\ \tilde{u}_{nq1} & \tilde{u}_{nq2} \end{bmatrix} \begin{bmatrix} \tilde{i}_{sd1} & \tilde{i}_{sd2} \\ \tilde{i}_{sq1} & \tilde{i}_{sq2} \end{bmatrix}^{-1} \tag{15}$$

where $\{\tilde{u}_{nd1}, \tilde{u}_{nq1}, \tilde{i}_{sd1}, \tilde{i}_{sq1}\}$ and $\{\tilde{u}_{nd2}, \tilde{u}_{nq2}, \tilde{i}_{sd2}, \tilde{i}_{sq2}\}$ are linearly independent. When deducing the dq-frame impedance of rectifier system with APF, the state-space averaging modeling of converters is applied. As can be seen from Tables V and VI in the Appendix, the switching frequency of rectifier f_r is much smaller than that of APF, so the impedance in (14) is effective until the perturbation frequency reaches $0.5f_r$. In the remainder of this section, the impedance verification is presented first, and then the impact factors of the impedance accuracy are explored and proved.

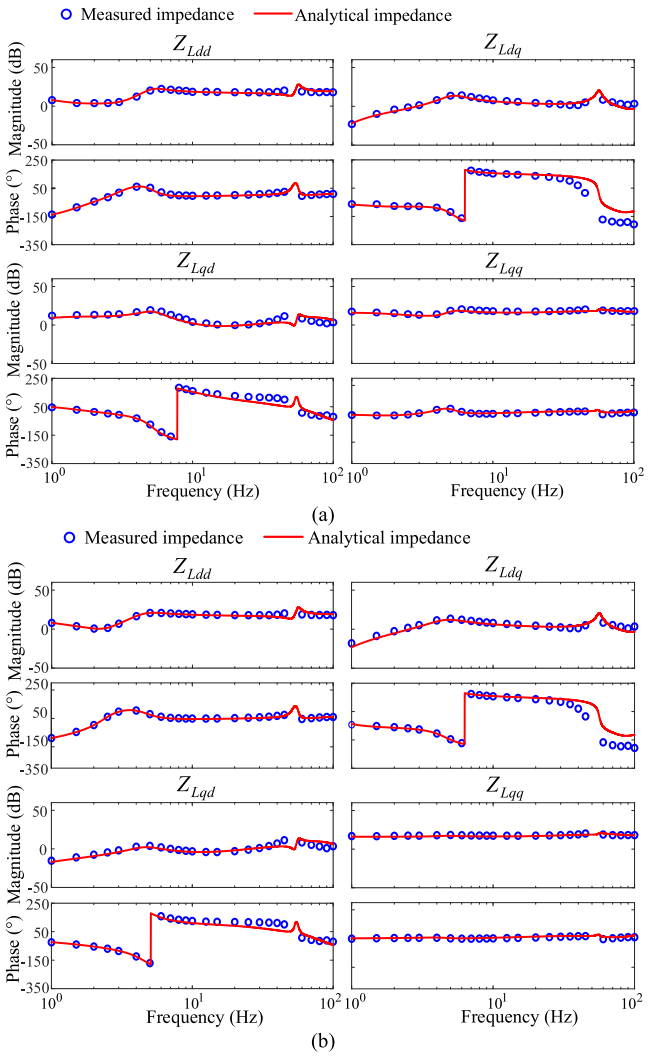

Fig. 10. Simulated and analytical impedance of rectifier system with APF. (a) Mode 1. (b) Mode 2.

A. Impedance Verification

Fig. 10 shows the simulated and derived impedance of the whole system when APF operates in two different modes mentioned before. The difference between the impedances in Fig. 10(a) and (b) mainly lies in the low-frequency region below 10 Hz, which indicates their different low-frequency characteristics that will be discussed in Section V. Besides, as can be seen, the derived impedances show good overall agreement with the simulated results when $f_p \leq 35$ Hz. There is a little difference for Z_{Ldq} when f_p is among [35 Hz, 100 Hz], while for Z_{Lqd} when f_p is among [35 Hz, 45 Hz]. In fact, the inconformity mainly results from the imprecise modeling of the duty ratio and the simplification of SOGI models, which will be further discussed in the following by taking the case where APF operates in Mode 1 for instance.

B. Impact of the Duty Ratio Model

As can be seen from the small-signal model of APF in Fig. 8, the duty ratio vector output by the controller is directly input to the main circuit. In other words, the α-axis component and β-axis component of the duty ratio both have impact on the main circuit, which is not consistent with the actual operation condition of single-phase APF where only the α-axis component is utilized to control the main circuit, as shown in Fig. 3. As mentioned before, to establish the *dq*-frame impedance model in single-phase system, the β-axis component of the duty ratio of APF is constructed 90° lagging behind the α-axis component. Hence, we can obtain

$$\begin{aligned}\tilde{\boldsymbol{d}}^s &= \begin{bmatrix}\tilde{d}_d^s \\ \tilde{d}_q^s\end{bmatrix} = \frac{1}{2\pi}\boldsymbol{T}_\theta * \left(\begin{bmatrix}1 & 0 \\ -j & 0\end{bmatrix} \cdot \begin{bmatrix}\tilde{d}_\alpha^{s'} \\ \tilde{d}_\beta^{s'}\end{bmatrix}\right) \\ &= \frac{1}{4\pi^2}\boldsymbol{T}_\theta * \left(\begin{bmatrix}1 & 0 \\ -j & 0\end{bmatrix} \cdot \left(\boldsymbol{T}_\theta^{-1} * \begin{bmatrix}\tilde{d}_d^{s'} \\ \tilde{d}_q^{s'}\end{bmatrix}\right)\right) \\ &= \boldsymbol{G}_{dd}\tilde{\boldsymbol{d}}^{s'}\end{aligned} \tag{16}$$

where $\tilde{\boldsymbol{d}}^{s'}$ is defined as the duty ratio vector output by the controller of APF. $\boldsymbol{G}_{dd}$ denotes the transfer matrix from $\tilde{\boldsymbol{d}}^{s'}$ to $\tilde{\boldsymbol{d}}^s$, which is measured in this article for further discussion.

C. Impact of the SOGI Models

In the following, the voltage SOGI of APF is taken for instance to illustrate the influence of SOGI model on the accuracy of system impedance. From Fig. 7, $\tilde{u}_{n\beta'}^s$ can be expressed as

$$\tilde{u}_{n\beta'}^s = \frac{\omega}{s} \cdot \tilde{u}_{n\alpha}^s = \frac{\omega}{s} \cdot \tilde{u}_n. \tag{17}$$

That is to say, when the grid voltage is perturbed by the cosine small signal u_{p1} in Fig. 9, we can obtain

$$\begin{bmatrix}\tilde{u}_{n\alpha 1}^s \\ \tilde{u}_{n\beta' 1}^s\end{bmatrix} = \begin{bmatrix}U_p \cos(\omega - \omega_p)t \\ \frac{\omega}{\omega - \omega_p} U_p \sin(\omega - \omega_p)t\end{bmatrix}. \tag{18}$$

The phase difference between $\tilde{u}_{n\alpha 1}^s$ and $\tilde{u}_{n\beta' 1}^s$ is 90°, but the amplitude of $\tilde{u}_{n\beta' 1}^s$ is $\omega/(\omega - \omega_p)$ times that of $\tilde{u}_{n\alpha 1}^s$. Hence, the actual input voltage vector $\tilde{\boldsymbol{u}}_{n1'}^s$ of the part in the blue dotted frame in Fig. 7 can be expressed as

$$\tilde{\boldsymbol{u}}_{n1'}^s = \begin{bmatrix}\tilde{u}_{nd1'}^s \\ \tilde{u}_{nq1'}^s\end{bmatrix} = \boldsymbol{T}_\theta \begin{bmatrix}\tilde{u}_{n\alpha 1}^s \\ \tilde{u}_{n\beta' 1}^s\end{bmatrix} = \boldsymbol{T}_\theta \begin{bmatrix}\tilde{u}_{n\alpha 1}^s \\ \frac{\omega}{\omega - \omega_p}\tilde{u}_{n\beta 1}^s\end{bmatrix} \tag{19}$$

where $\tilde{u}_{n\beta 1}^s$ denotes the component directly generated via lagging $\tilde{u}_{n\alpha 1}^s$ by 90°, namely $\tilde{u}_{n\beta 1}^s(s) = -j\tilde{u}_{n\alpha 1}^s(s)$,which also conforms to the definition of the virtual β-axis signal introduced in Section III-A. Ignoring the *d*-axis and *q*-axis components at frequency $2f - f_p$ of $\tilde{\boldsymbol{u}}_{n1'}^s$ in (19), we get

$$\begin{bmatrix}\tilde{u}_{nd1'}^s \\ \tilde{u}_{nq1'}^s\end{bmatrix} = \left(1 + \frac{1}{2} \cdot \frac{\omega_p}{\omega - \omega_p}\right) \begin{bmatrix}U_p \sin(\omega_p)t \\ U_p \cos(\omega_p)t\end{bmatrix} = k^- \begin{bmatrix}\tilde{u}_{nd1}^s \\ \tilde{u}_{nq1}^s\end{bmatrix} \tag{20}$$

where k^- is defined as the error coefficient. In Section III, to derive the transfer matrix of voltage SOGI in *dq* frame, the amplitudes of $\tilde{u}_{n\beta'}^s$ and $\tilde{u}_{n\alpha}^s$ are regarded as the same, namely k^- is equal to 1. In this regard, the relationship between the real transfer matrix $\boldsymbol{H}_{udq-}$ and the analytical transfer matrix $\boldsymbol{H}_{udq}$ of the voltage SOGI can be expressed as

$$\boldsymbol{H}_{udq-} = k^- \boldsymbol{H}_{udq}. \tag{21}$$

Similarly, when the grid voltage is perturbed by the cosine small signal u_{p2} in Fig. 9, the real transfer matrix $\boldsymbol{H}_{udq+}$ of voltage SOGI can be derived as

$$\boldsymbol{H}_{udq+}=\left(1-\frac{1}{2}\cdot\frac{\omega_p}{\omega+\omega_p}\right)\cdot\boldsymbol{H}_{udq}=k^{+}\boldsymbol{H}_{udq}. \quad (22)$$

From (21) and (22), we can see that, in dq frame, the real transfer matrix of voltage SOGI at frequency f_p is not unique. When the method in Fig. 9 is utilized for dq-frame impedance measurement, we can obtain the relationship between the input signal $[\tilde{\boldsymbol{u}}^s_{n1}\ \tilde{\boldsymbol{u}}^s_{n2}]$ and the response signal of the voltage SOGI $[\tilde{\boldsymbol{u}}^{s'}_{n1}\ \tilde{\boldsymbol{u}}^{s'}_{n2}]$ as (23). $\boldsymbol{K}$ is defined as the error coefficient matrix, which is ignored in the SOGI model derived in Section III

$$\begin{aligned}\left[\tilde{\boldsymbol{u}}^{s'}_{n1}\ \tilde{\boldsymbol{u}}^{s'}_{n2}\right]&=\begin{bmatrix}\tilde{u}^{s'}_{nd1}&\tilde{u}^{s'}_{nd2}\\ \tilde{u}^{s'}_{nq1}&\tilde{u}^{s'}_{nq2}\end{bmatrix}=\begin{bmatrix}\tilde{u}^{s'}_{nd1}\\ \tilde{u}^{s'}_{nq1}\end{bmatrix}\begin{bmatrix}1&0\end{bmatrix}+\begin{bmatrix}\tilde{u}^{s'}_{nd2}\\ \tilde{u}^{s'}_{nq2}\end{bmatrix}\begin{bmatrix}0&1\end{bmatrix}\\&=\boldsymbol{H}_{udq}k^{-}\begin{bmatrix}\tilde{u}^{s}_{nd1}\\ \tilde{u}^{s}_{nq1}\end{bmatrix}\begin{bmatrix}1&0\end{bmatrix}+\boldsymbol{H}_{udq}k^{+}\begin{bmatrix}\tilde{u}^{s}_{nd2}\\ \tilde{u}^{s}_{nq2}\end{bmatrix}\begin{bmatrix}0&1\end{bmatrix}\\&=\boldsymbol{H}_{udq}\underbrace{\begin{bmatrix}\tilde{u}^{s}_{nd1}&\tilde{u}^{s}_{nd2}\\ \tilde{u}^{s}_{nq1}&\tilde{u}^{s}_{nq2}\end{bmatrix}}_{\left[\tilde{\boldsymbol{u}}^{s}_{n1}\ \tilde{\boldsymbol{u}}^{s}_{n2}\right]}\underbrace{\begin{bmatrix}k^{-}&0\\0&1\end{bmatrix}\begin{bmatrix}1&0\\0&k^{+}\end{bmatrix}}_{\boldsymbol{K}}.\end{aligned} \quad (23)$$

D. Verification of the Impact Factors

In the following, the influence of SOGI model and duty ratio model on the impedance accuracy of APF is discussed. To simply the analysis, the single rectifier is replaced with an inductive load $Z_{lo}=R_{lo}+sL_{lo}$, whose impedance in dq frame can be expressed as (24). In this case, the region of system impedance inconformity is consistent with that in Fig. 10, which will not be elaborated upon

$$\boldsymbol{Z}_{re}=\boldsymbol{Z}_{load}=\begin{bmatrix}Z_{lodd}&Z_{lodq}\\ Z_{loqd}&Z_{loqq}\end{bmatrix}=\begin{bmatrix}R_{lo}+sL_{lo}&-\omega L_{lo}\\ \omega L_{lo}&R_{lo}+sL_{lo}\end{bmatrix}. \quad (24)$$

When the grid voltage is perturbed by the cosine small signal u_{p1}, the dq-frame impedance of the APF system considering the accurate models of SOGIs and duty ratio can be presented as (25), where $\boldsymbol{A}$, $\boldsymbol{B}$, and $\boldsymbol{C}$ are the multiplication results of multiple transfer matrices, which are presented in the Appendix. It is noted that only $\boldsymbol{C}$ is independent of the transfer matrix $\boldsymbol{G}_{dd}$, so it is utilized as the index to further validate the impact factors of impedance accuracy in this part

$$\begin{aligned}\boldsymbol{Z}^{-}_{apf}=&(((\boldsymbol{G}_{id}(\boldsymbol{I}_{2x2}+\boldsymbol{G}_{dd}\boldsymbol{G}_{del}\boldsymbol{G}_{ci}\boldsymbol{G}_{dc}k_{dc}\boldsymbol{G}_{ud})^{-1}\\&\times\boldsymbol{G}_{dd}\boldsymbol{G}_{del}\boldsymbol{G}_{ci}((\boldsymbol{k}_{ic}\\&-\boldsymbol{H}_{lf}k^{-}\boldsymbol{H}_{icdq}\boldsymbol{k}_{ic})\boldsymbol{Z}^{-1}_{re}\\&-(\boldsymbol{G}^{icc}_{pll}+\boldsymbol{H}_{lf}\boldsymbol{G}^{ic}_{pll})k^{-}\boldsymbol{H}_{udq}\boldsymbol{k}_{un}-\boldsymbol{G}_{dc}\\&\cdot k_{dc}\boldsymbol{G}_{uu})+\boldsymbol{Z}^{-1}_{fp})^{-1}(\boldsymbol{I}_{2x2}-\boldsymbol{G}_{id}\\&\cdot(\boldsymbol{I}_{2x2}+\boldsymbol{G}_{dd}\boldsymbol{G}_{del}\boldsymbol{G}_{ci}\boldsymbol{G}_{dc}k_{dc}\\&\cdot\boldsymbol{G}_{ud})^{-1}\boldsymbol{G}_{dd}\boldsymbol{G}_{del}\boldsymbol{G}_{ci}\boldsymbol{k}_{in}))^{-1}+\boldsymbol{Z}^{-1}_{re})^{-1}\\=&(\boldsymbol{A}+k^{-}\boldsymbol{B}\boldsymbol{C}+\boldsymbol{Z}^{-1}_{re})^{-1}.\end{aligned} \quad (25)$$

For this case, the relationship between the grid voltage $\tilde{\boldsymbol{u}}^s_{n1}$ and grid current $\tilde{\boldsymbol{i}}^s_{s1}$ can be expressed as

$$\tilde{\boldsymbol{u}}^s_{n1}=\boldsymbol{Z}^{-}_{apf}\tilde{\boldsymbol{i}}^s_{s1}=(\boldsymbol{A}+k^{-}\boldsymbol{B}\boldsymbol{C}+\boldsymbol{Z}^{-1}_{re})^{-1}\tilde{\boldsymbol{i}}^s_{s1} \quad (26)$$

which yields that

$$k^{-}\boldsymbol{C}\cdot\tilde{\boldsymbol{u}}^s_{n1}=\boldsymbol{B}^{-1}\cdot\tilde{\boldsymbol{i}}^s_{s1}-(\boldsymbol{B}^{-1}\boldsymbol{Z}^{-1}_{re}+\boldsymbol{B}^{-1}\boldsymbol{A})\tilde{\boldsymbol{u}}^s_{n1}. \quad (27)$$

Similarly, when the grid voltage is perturbed by the cosine small signal u_{p2}, we can obtain

$$\tilde{\boldsymbol{u}}^s_{n2}=\boldsymbol{Z}^{+}_{apf}\tilde{\boldsymbol{i}}^s_{s2}=(\boldsymbol{A}+k^{+}\boldsymbol{B}\boldsymbol{C}+\boldsymbol{Z}^{-1}_{re})^{-1}\tilde{\boldsymbol{i}}^s_{s2} \quad (28)$$

namely

$$k^{+}\boldsymbol{C}\cdot\tilde{\boldsymbol{u}}^s_{n2}=\boldsymbol{B}^{-1}\cdot\tilde{\boldsymbol{i}}^s_{s2}-(\boldsymbol{B}^{-1}\boldsymbol{Z}^{-1}_{re}+\boldsymbol{B}^{-1}\boldsymbol{A})\tilde{\boldsymbol{u}}^s_{n2}. \quad (29)$$

Combining (27) and (29) yields (30) shown at the bottom of this page.

To verify the impact factors of the impedance accuracy aforementioned, $\boldsymbol{C}$ is calculated theoretically and $\boldsymbol{C}_{acu}$ is calculated based on the expression on the right of (30), where the response voltages $[\tilde{\boldsymbol{u}}^s_{n1}\ \tilde{\boldsymbol{u}}^s_{n2}]$ and currents $[\tilde{\boldsymbol{i}}^s_{s1}\ \tilde{\boldsymbol{i}}^s_{s2}]$ are all obtained via measurement. Specifically, if $\boldsymbol{C}_{acu}$, which is termed as the measured result here, is in accordance with the theoretical calculation result $\boldsymbol{C}$, namely (30) holds, the correctness of (26) and (28) can be well proved. For the closed-loop impedance of APF derived in Section III, the error coefficient matrix $\boldsymbol{K}$ and the transfer matrix $\boldsymbol{G}_{dd}$ are not taken into consideration. That is to say, they are both regarded as the 2-by-2 identity matrices. In this situation, the result measured based on the expression on the right of (30) is defined as $\boldsymbol{C}_{err}$. As shown in Fig. 11, $\boldsymbol{C}_{acu}$ matches well with the analytical result $\boldsymbol{C}$, but $\boldsymbol{C}_{err}$ not. Therefore, the partial impedance inconformity in Fig. 10 is proved to result from the simplification of SOGI model and the imprecise modeling of duty ratio, which is also a gap in existing articles. Since the derived impedance matches well with the simulated results when $f_p\le 35$ Hz, it can be utilized to assess the system low-frequency stability with enough accuracy in this article.

V. Low-Frequency Stability Analysis

In this section, the impact of CHB multilevel APF on the stability of rectifier system is revealed based on the source-load system shown in Fig. 4. It is noted that the dq-frame impedance of the load subsystem relies on the amplitude of the voltage at PCC in stable state, which needs to be calculated according to the principle of active power balance and system impedance triangle. In the following, the stability of rectifier system and its sensitivity to parameters in different cases after APF is

$$\boldsymbol{C}=\underbrace{(\boldsymbol{B}^{-1}\cdot[\tilde{\boldsymbol{i}}^s_{s1}\quad\tilde{\boldsymbol{i}}^s_{s2}]-\boldsymbol{B}^{-1}(\boldsymbol{Z}^{-1}_{re}+\boldsymbol{A})[\tilde{\boldsymbol{u}}^s_{n1}\quad\tilde{\boldsymbol{u}}^s_{n2}])\cdot([\tilde{\boldsymbol{u}}^s_{n1}\quad\tilde{\boldsymbol{u}}^s_{n2}]\boldsymbol{K})^{-1}}_{\boldsymbol{C}_{acu}} \quad (30)$$

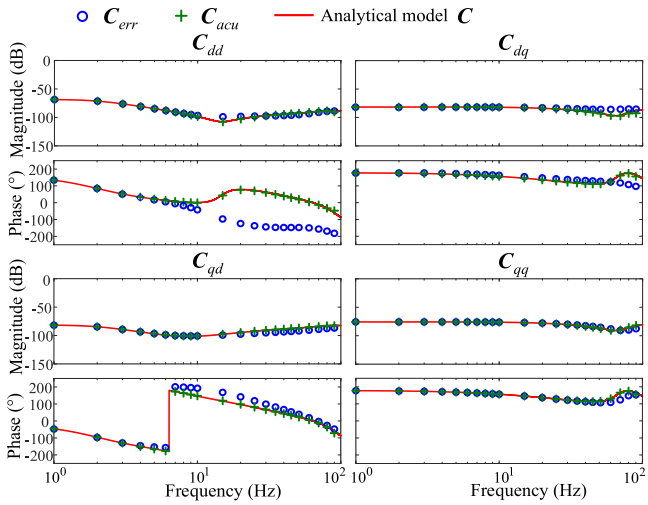

Fig. 11. Simulated and analytical transfer matrix.

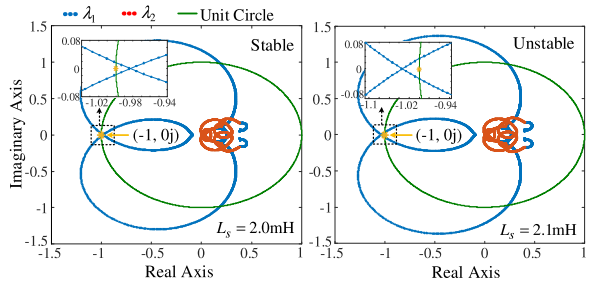

Fig. 12. Nyquist plots without APF.

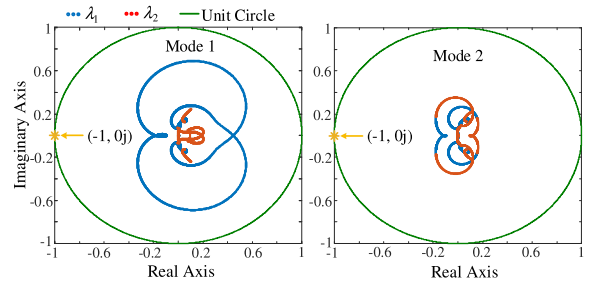

Fig. 13. Nyquist plots with APF when $L_s = 2.1$ mH.

introduced are estimated and compared by means of GNSC and power consumption criterion.

A. Stability Enhancement With APF

It is reported that the higher the grid inductance L_s, the more likely the LFO [6]. Hence, L_s is adjusted high enough so that LFO can happen when one rectifier is energized. Fig. 12 presents the Nyquist plots of rectifier system without APF. The green line denotes the unit circle, on which the yellow point denotes $(-1, 0j)$. It can be observed that the system is marginally stable when L_s is increased to 2.0 mH. As shown in Fig. 13, after APF is hooked up to the grid, the Nyquist plot becomes far away from the critical point $(-1, 0j)$, especially when APF operates in Mode 2, which indicates that the stability margin of rectifier system can be significantly enhanced with APF. Fig. 14 compares the

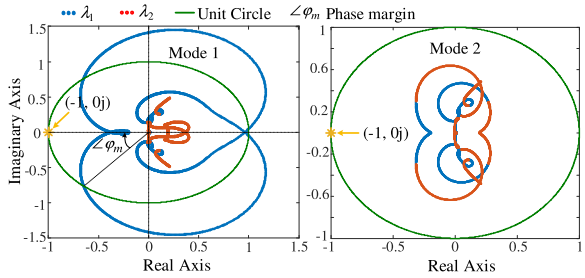

Fig. 14. Nyquist plots with APF when $L_s = 4.2$ mH.

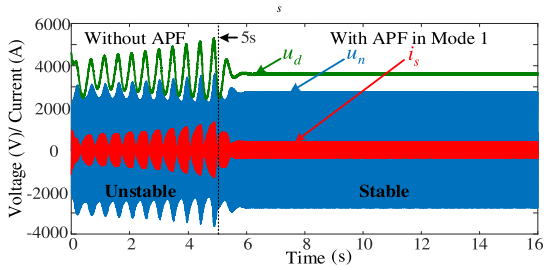

Fig. 15. Simulated waveforms of u_d, u_n and i_s when $L_s = 2.1$ mH.

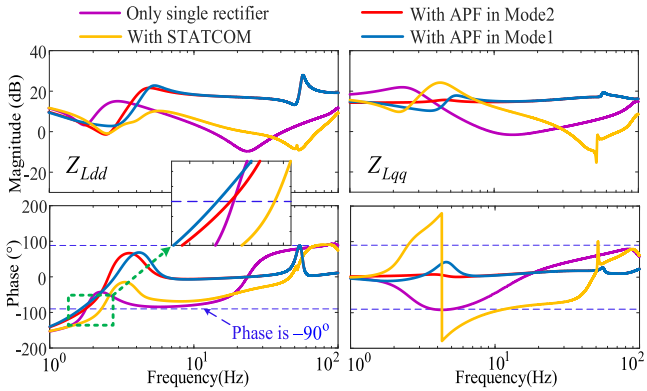

Fig. 16. Impedance diagrams of Z_{Ldd} and Z_{Lqq} under four different conditions.

Nyquist plots when APF operates in two different modes with L_s increased to 4.2 mH. As can be seen, in Mode 1, the system is stable with the phase margin only 49.7°, while in Mode 2, the Nyquist plot is disjoint from the unit circle and the phase margin remains large enough. That is to say, the combination of reactive and interharmonic compensation can maximize the system stability margin. Fig. 15 shows the simulated results when $L_s = 2.1$ mH, where APF is energized in Mode 1 at 5 s. The LFO in rectifier system is well eliminated with APF, as predicted from the Nyquist plot in Fig. 13.

As reported in [16], for the rectifier system in CRH5 EMUs, broader frequency range of negative impedance on Z_{Ldd} will be more likely to cause LFO. In [8], the STATCOM is designed to improve the stability of the rectifier system to eliminate the LFO. However, combining the research in [8] and this article, it is found that the negative impedance range of rectifier system becomes wider with STATCOM, while that becomes narrower with the APF proposed in this article, as shown in Fig. 16. It indicates that there is no significant relationship between the

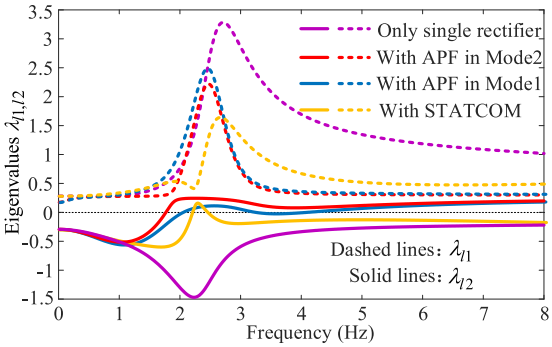

Fig. 17. Eigenvalues of $\boldsymbol{Y}_H$ under four different conditions.

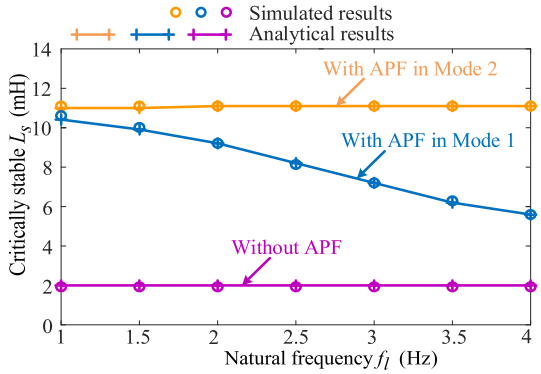

Fig. 18. Critically stable inductance L_s when the natural frequency f_l changes.

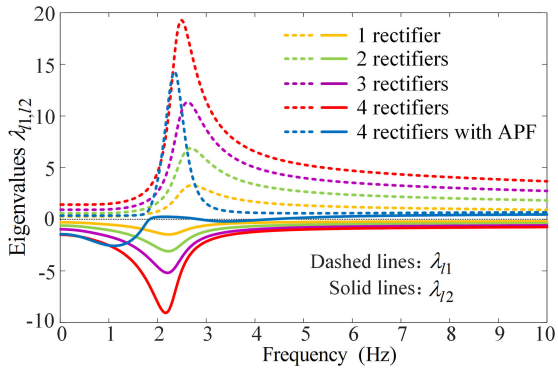

Fig. 19. Eigenvalues of $\boldsymbol{Y}_H$ when the number of rectifiers m varies.

negative impedance range and the stability of the rectifier system in this situation. In fact, given that the grid is evidently passive, the oscillation at a certain frequency will not occur if the load subsystem consumes active power at this frequency [11], [20]. Hence, to further elucidate the impact of APF on the rectifier system, a criterion for system power consumption is applied here. Regarding each component of $\tilde{\boldsymbol{u}}_n^s$ and $\tilde{\boldsymbol{i}}_s^s$ as a complex phasor, the input active power P at the PCC can be expressed as

$$P = \frac{1}{2}\mathrm{Re}\left\{\tilde{u}_{nd}^s \tilde{i}_{sd}^{s*} + \tilde{u}_{nq}^s \tilde{i}_{sq}^{s*}\right\} = \frac{1}{4}(\tilde{\boldsymbol{u}}_n^{sH}\tilde{\boldsymbol{i}}_s^s + \tilde{\boldsymbol{i}}_s^{sH}\tilde{\boldsymbol{u}}_n^s) \quad (31)$$

where the superscript $*$ and H mean the complex conjugate and conjugate transpose, respectively. Based on the relationship between $\tilde{\boldsymbol{u}}_n^s$ and $\tilde{\boldsymbol{i}}_s^s$, we can obtain

$$\tilde{\boldsymbol{u}}_n^{sH}\tilde{\boldsymbol{i}}_s^s + \tilde{\boldsymbol{i}}_s^{sH}\tilde{\boldsymbol{u}}_n^s = \tilde{\boldsymbol{u}}_n^{sH}[\boldsymbol{Y}_{apf} + \boldsymbol{Y}_{apf}^H]\tilde{\boldsymbol{u}}_n^s = \tilde{\boldsymbol{u}}_n^{sH}\boldsymbol{Y}_H\tilde{\boldsymbol{u}}_n^s \quad (32)$$

where the right-side part is a Hermitian quadratic form with the Hermitian matrix

$$\boldsymbol{Y}_H = \begin{bmatrix} a & b^* \\ b & d \end{bmatrix} = \begin{bmatrix} 2\mathrm{Re}(Y_{Ldd}) & Y_{Ldq} + Y_{Lqd}^* \\ Y_{Ldq}^* + Y_{Lqd} & 2\mathrm{Re}(Y_{Lqq}) \end{bmatrix}. \quad (33)$$

According to the properties of Hermitian matrix, all the eigenvalues of $\boldsymbol{Y}_H$ are real [21]. When $\boldsymbol{Y}_H$ is positive definite, (32) is positive, that is, the positive active power is consumed. This situation holds if and only if both of the eigenvalues of $\boldsymbol{Y}_H$ are positive. Here, the natural frequency of LPF in q channel is set as 1.5 Hz for sharper contrast. Fig. 17 shows the eigenvalues of $\boldsymbol{Y}_H$ at low frequencies (0.01–8 Hz) under four different situations, where the black dashed line presents that the eigenvalue is equal to zero. It is observed that the frequency region of negative eigenvalue λ_{l2} is significantly narrowed with APF, especially when APF operates in Mode 2. The yellow lines present the eigenvalues of $\boldsymbol{Y}_H$ when the STATCOM proposed in [8] is hooked up to the grid. In this case, the range of negative eigenvalues is reduced but to a relatively limited extent. The positive eigenvalues are distributed around 2.2 Hz, which is also the frequency of LFO in the rectifier system.

B. Parameters and Sensitivity Analysis

As shown in Fig. 3, the LPFs play a key role in the performance of the interharmonic and reactive current detector of APF, which are able to further influence the stability margin of the whole system. In this part, the natural frequencies (also named as the bandwidths) of the two LPFs in APF are both set as f_l. Fig. 18 shows the critically stable inductance L_s as the natural frequency f_l varies. As can be seen, the rectifier system with APF in Mode 1 is sensitive to f_l. Lower f_l is prone to bigger system stability margin. When APF operates in Mode 2, f_l seems to have little influence on the system. Actually, larger f_l can aggravate the system sensitivity to the parameters of rectifier, which is undesired, so f_l is usually set to a relatively small value. In addition, from Fig. 18 we can observe that the simulated results are almost consistent with the analytical ones, which indicates that the stability analysis with GNSC based on the impedance derived in Section III performs well. Similarly, the impact of the dc voltage controller, current controller, and PLL of APF on the system stability can also be evaluated. It is worth noting that, under different controller parameters of APF, the rectifier system has certain differences in its own parameter sensitivity. The curves of eigenvalues of $\boldsymbol{Y}_H$, which appear relatively intuitive, can be combined with GNSC for comprehensive comparisons and analysis.

Fig. 19 shows the eigenvalues of $\boldsymbol{Y}_H$ when different number of rectifiers are hooked up to the grid for further discussion, where L_s is fixed at 1.0 mH. It can be seen that, as the number of energized rectifiers m is increased, the curve of eigenvalue λ_{l2} gradually moves far away from the black horizontal border line and the frequency region where λ_{l2} presents negative becomes increasingly apparent. As shown in Table I, the state of rectifier system changes from obviously stable to obviously unstable

TABLE I
LOW-FREQUENCY STABILITY ANALYSIS BASED ON GNSC

m	1	2	3	4
Without APF	Obviously stable	Marginally stable	Obviously unstable	Obviously unstable
With APF in Mode 2	Obviously stable	Obviously stable	Obviously stable	Obviously stable

TABLE II
CRITICALLY STABLE L_S UNDER DIFFERENT CONDITIONS

Rectifier parameters	-	k_{Pic}	k_{Iic}	k_{Puc}	k_{Iuc}
Original value	-	1.65	50	0.8	5
Changed value	-	1.2	88	3	10
Critical L_s (Single rectifier)	&1	2mH	2mH	2mH	2mH
	&2	0.8mH	0.6mH	1.7mH	0.7mH
Reduction rate	-	60%	70%	15%	65%
Critical L_s (With STATCOM)	&1	9.2mH	9.2mH	9.2mH	9.2mH
	&2	6.4mH	2.1mH	6.9mH	7.2mH
Reduction rate	-	30.4%	77.2%	25%	21.7%
Critical L_s (With APF--Mode 2)	&1	11.1mH	11.1mH	11.1mH	11.1mH
	&2	10.5mH	10.6mH	11.1mH	10.2mH
Reduction rate	-	5.4%	4.5%	0%	8.1%

Notes: &1 and &2 represent the critically stable value of L_s before and after the parameters of rectifier change, respectively.

in this situation, which indicates that larger m will worsen the stability of rectifier system. However, after APF is introduced in Mode 2, the whole system can always maintain excellent performance with a sufficient stability margin.

In Table II, the critically stable values of L_s of single rectifier system under different parameters are compared and analyzed. The parameters of APF and rectifier are set based on Tables V and VI. As can be seen, with the STATCOM proposed in [8], the stability of rectifier system is improved obviously but still greatly influenced by its PI parameters. For instance, when k_{Pic} is changed to 1.2, the reduction rate of L_s reaches up to 30.4%. In contrast, after APF is introduced, the rectifier system is no longer sensitive to k_{Pic}, k_{Iic}, $k_{Puc,}$ and k_{Iuc}, the stability margin of which can always be maintained at a high level, which indicates that the APF proposed in this article owns much better performance than the STATCOM in [8].

VI. SIMULATION ANALYSIS

In order to verify the LFO suppression effect of CHB multilevel APF in Mode 2, simulations in MATLAB are implemented in this section. As shown in Fig. 20, the equivalent grid impedance is composed of an inductor L_s and a resistor R_s. Multiple CRH5 EMUs are hooked up to the grid in turn via the breakers. Fig. 21 describes the waveforms of u_n, i_s, and u_d before APF is put into operation. As can be seen, when $L_s = 9.0$ mH, the system can always maintain stable with a small constant phase difference between the grid voltage and current, which is caused by the vehicle transformers that consume the reactive power in grid. After L_s is increased, LFO occurs when the eighth vehicle

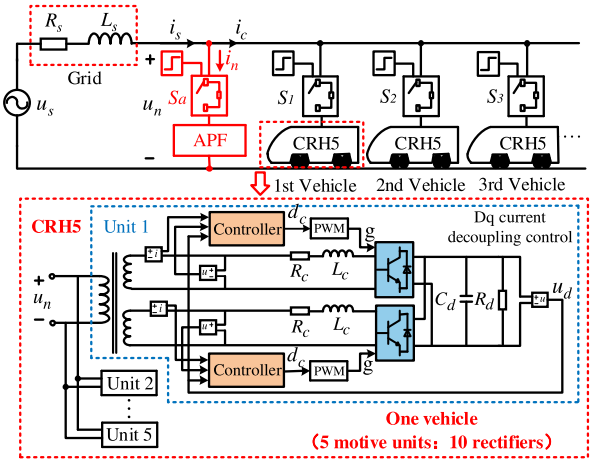

Fig. 20. Simulation model of vehicle-grid system with APF.

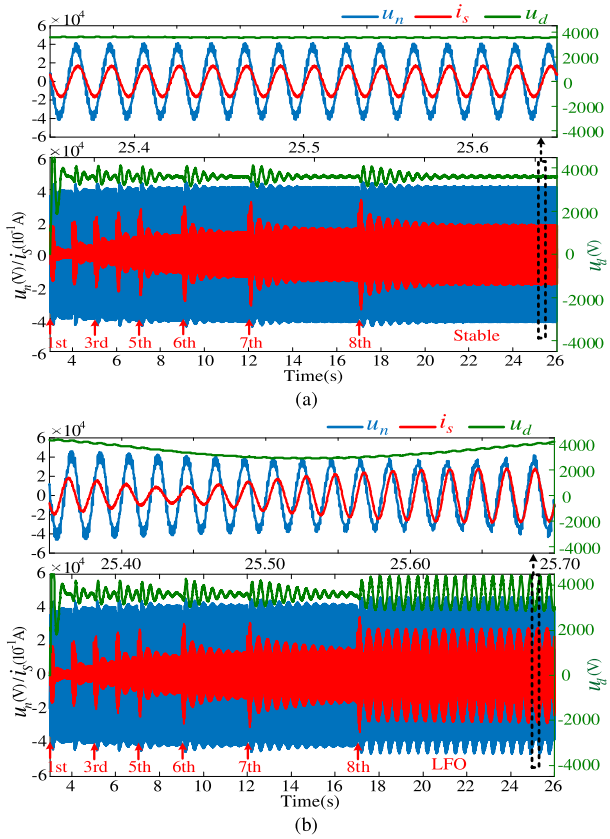

Fig. 21. Simulated waveforms without APF. (a) $L_s = 9.0$ mH; (b) $L_s = 9.8$ mH.

is accessed to the grid at 17 s. The dc-side voltage, grid voltage, and grid current all fluctuate with high magnitudes. The partial enlarged view at the top of Fig. 21(b) indicates that the phase difference between the grid current and grid voltage consistently varies. Sometimes the reactive power in grid is inductive and sometimes capacitive. In consequence, the increase of L_s or the number of vehicles accessed will worsen the stability of vehicle-grid system and lead to LFO. From Fig. 22, we can observe that the low-frequency instable phenomenon is avoided by introducing APF in Mode 2. The system maintains stable with

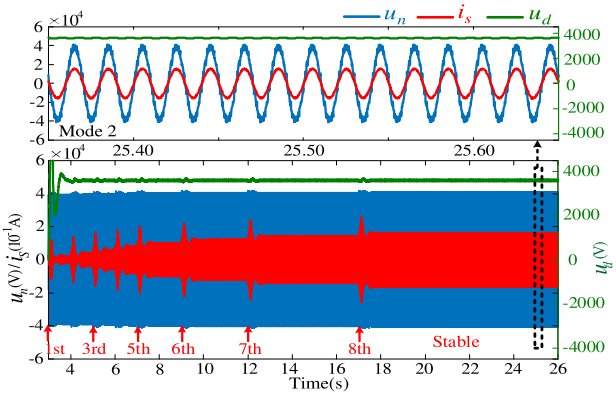

Fig. 22. Simulated waveforms with APF in Mode 2 when $L_s = 9.8$ mH.

TABLE III
PERFORMANCE COMPARISON OF ELECTRICAL QUANTITIES

Items	Fluctuation of u_d	Fluctuation of u_n	THD of i_s
Without APF	±750V	±4050V	60.18%
With APF	±30V	±7V	3.43%

eight vehicles in operation. Due to the reactive compensation of APF, the grid current and grid voltage can always keep in phase at steady state. Table III shows the total harmonic distortion (THD) of grid current and the fluctuation of grid voltage peak value and dc-side voltage for the cases in Figs. 21(b) and 22. It can be seen that all the three electrical quantities are obviously improved with APF. In consequence, APF can restrain the LFO and enhance the stability of vehicle-grid system effectively.

VII. EXPERIMENTAL VERIFICATION

To further verify the accuracy of theoretical analysis and the feasibility of CHB multilevel APF in LFO inhibition, experiments are implemented on the controller HIL platform.

A. HIL Simulation Platform

Fig. 23(a) shows the diagram of the whole experimental system. The grid is represented by the Thewenin equivalent circuit in the red dotted frame. Here, six single-phase rectifiers in CRH5 EMUs are determined to simulate six vehicles, so as to verify the LFO suppression effect of APF under the condition of multiple vehicles accessed. i_{cm} ($m = 1, 2, \ldots, 6$) denotes the input current of the mth vehicle. The parameters of vehicles and APF are listed in Tables V and VI in the Appendix, respectively. As shown in Fig. 23, the grid and the main circuit models of vehicles and APF are developed via the electromagnetic transient simulation software StarSim in the host computer and operate on the NI-PXIe-FPGA-7868R based real-time HIL system with 1 μs time step. The NI-PXIe-8821-7846R based rapid control prototyping (RCP) is a real-time industrial controller, which is responsible for sampling the voltage and current signals of main circuits, running the control algorithms of vehicles and APF and outputting the digital control signals to the main circuits in the real-time simulator. The sampling frequency of real-time controller is selected as 20 kHz. In addition, the green boards in

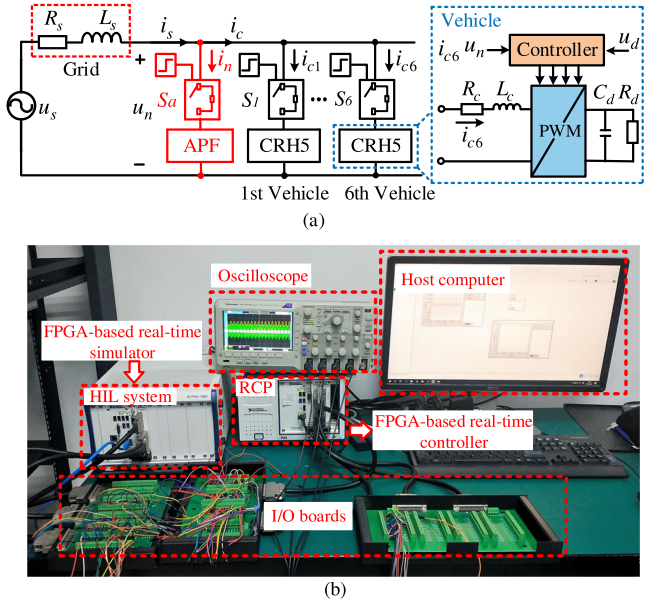

Fig. 23. Experimental setup. (a) Diagram of the experimental model. (b) View of controller HIL simulation platform.

TABLE IV
EXPERIMENTAL RESULTS UNDER DIFFERENT CONDITIONS

Cases	Without APF	APF runs in Mode 1	APF runs in Mode 2
L_s=2.1mH	Divergent LFO	Stable	Stable
L_s=4.2mH	System crashes	Stable	Stable

Fig. 23(b) contain multiple I/O channels, which are utilized to realize the analog/digital signals interaction between the RCP and the real-time simulation system from the physical level. The oscilloscope can record the waveforms of grid voltage, grid current as well as dc-side voltage. The user interface of the host computer can provide all the related data as well as the measurements of the whole system.

B. Experimental Results

First of all, one vehicle, which is actually one single-phase rectifier here, is energized for the stability analysis. Table IV lists the results obtained based on the experimental waveforms when L_s is set to 2.1 and 4.2 mH, respectively. As can be observed, without APF, the LFO in rectifier system appears when L_s is only 2.1 mH and larger L_s makes the system crash faster. As APF is introduced in two different modes, the LFO is eliminated effectively and the system can always operate stably. Fig. 24 shows the Nyquist plots drawn based on the measured impedance model under the conditions in Fig. 14. It is seen that, compared with the APF in Mode 1, the APF in Mode 2 presents superior performance in improving the system stability. Moreover, all the results in Table IV and Fig. 24 accord with that in Figs. 12, 13, and 14, which indicates that the theoretical analysis based on the derived impedance in Section V shows good accuracy.

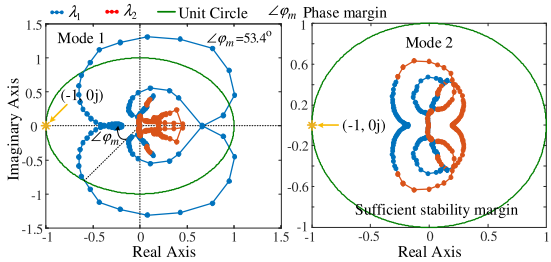

Fig. 24. Nyquist plots drawn based on the test data.

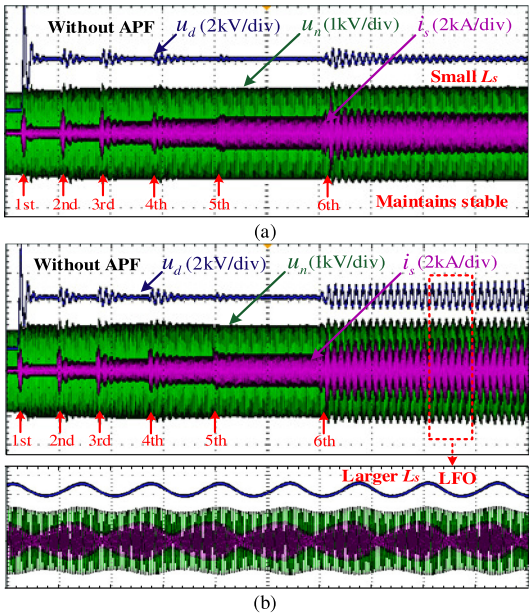

Fig. 25. Experimental waveforms of u_d, u_n, and i_s without APF. (a) $L_s = 0.30$ mH; (b) $L_s = 0.33$ mH.

Fig. 25 shows the waveforms of dc-side voltage u_d, grid current i_s, and grid voltage u_n when six vehicles are successively energized without APF via the breakers. Consistent with the conclusion previously illustrated, the LFO is more easily to be triggered with larger L_s or larger number of vehicles accessed. From Fig. 25(b), it can be seen that the system enters into a low-frequency unstable state once the sixth vehicle is put into operation. The amplitudes of grid voltage and grid current as well as the dc-side voltage all fluctuate consistently. After APF is hooked up to the grid in Mode 2, the system is able to maintain stability, as shown in Fig. 26. The dc-side voltage tracks well to the reference value 3600 V given in the controller with small deviation. From the enlarged view, we can observe that the grid current and grid voltage are always in phase, which implies that the whole system is able to operate under unit power factor. In other words, the APF is fully capable of restraining the LFO in vehicle-grid system.

VIII. Conclusion

In order to restrain the LFO and improve the stability of vehicle-grid system, a single-phase CHB multilevel APF is designed, which can reshape the load impedance without any change on the rest parts of the system. First, the current tracking

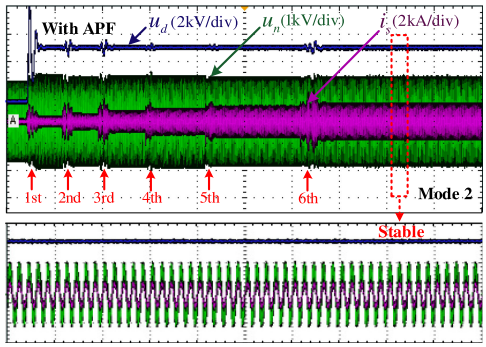

Fig. 26. Experimental waveforms of u_d, u_n, and i_s with APF when $L_s = 0.33$ mH.

controller of APF is transformed into *dq* frame via equivalence, and the *dq*-frame impedance model of rectifier system with APF is established. The impact of SOGI model and duty ratio model on the impedance accuracy is explored and verified by comparing the analytical results with the measured results in MATLAB. Then, based on GNSC and system power consumption criterion, the system stability margins in different cases and their sensitivity to the parameters of rectifier system are assessed. In addition, the superior performance of APF in LFO elimination is demonstrated by the time-domain simulations and the experiments on the controller HIL platform. In the following, some pivotal conclusions are drawn.

1) The *dq*-frame impedance of rectifier system with APF derived based on the equivalent main circuit and control model is accurate enough for low-frequency stability analysis. The partial deviation in the impedance diagonal elements Z_{Ldq} and Z_{Lqd} mainly results from the imprecise modeling of the duty ratio and simplified model of SOGI in *dq* frame. The relevant research of Sections IV-B to D provides some insights and method references for the error analysis and verification of *dq*-frame impedance model of single-phase systems, which can help us to judge the applicability of *dq*-frame impedance modeling approach for the system in specific situations.
2) The frequency region of negative eigenvalue λ_{l2} of $\boldsymbol{Y}_H$ can be significantly narrowed with APF in two different modes, but to a relatively limited extent with the STATCOM in [8].
3) APF can provide dynamic interharmonic and reactive compensation and eliminate the LFO in vehicle-grid system effectively. Based on the theoretical analysis in Section V, it is proved that the stability margin of rectifier system can be significantly enhanced with APF regardless of the parameters settings of the rectifiers, which owns much better performance than the STATCOM proposed in [8].
4) Compared with Mode 1, Mode 2 enables APF to raise the stability margin of rectifier system to a higher level. That is to say, the combination of reactive and interharmonic compensation is able to maximize the system stability margin.

5) The curves of eigenvalues of $\boldsymbol{Y}_H$ appearing relatively intuitive can be combined with GNSC for comprehensive analysis to explore the impact of APF and its different parameters on the stability of rectifier system, which is benefit for APF designing.

In conclusion, as an approach for load impedance reshaping, the CHB multilevel APF is proposed in this article to eliminate the LFO in vehicle-grid system. The *dq*-frame impedance modeling process and stability analysis of the whole system are presented, which can provide available guidelines on practical applications.

APPENDIX

The expression of $\boldsymbol{G}_{uu}, \boldsymbol{G}_{ud}, \boldsymbol{G}_{id}, \boldsymbol{Z}_{fp}^{-1}, \boldsymbol{Z}_{re}^{-1}, G_{pll}, \boldsymbol{A}, \boldsymbol{B}$ and $\boldsymbol{C}$ are presented as follows:

TABLE V
PARAMETERS OF THE RECTIFIER

Quantity	Symbol	Values
Switching frequency	f_r	250Hz
Vehicle transformer inductance	L_c	5.4mH
Vehicle transformer resistance	R_c	0.145Ω
DC-link voltage reference	U_d	3600V
DC-link capacitance	C_d	9mF
Equivalent load	R_d	25Ω
PLL controller	k_{Ppc}, k_{Ipc}	0.7, 25
Current controller	k_{Pic}, k_{Iic}	1.65, 50
DC voltage controller	k_{Puc}, k_{Iuc}	0.8, 5

TABLE VI
PARAMETERS OF THE GRID AND APF

Quantity	Symbol	Values
Input voltage	U_{srms}	1947V
DC voltage reference of SMs	U_{dc}	575V
DC capacitance of SMs	C_n	20mF
Carrier frequency	f_k	3000Hz
LPF in *d* channel	f_{l1}, Q_{damp1}	2Hz, 0.707
LPF in *q* channel	f_{l2}, Q_{damp2}	2Hz, 0.707
PLL controller	k_{Ppll}, k_{Ipll}	0.7, 25
Current controller	k_{Pi}, k_{Ii}	0.8, 1
DC voltage controller	k_{Pu}, k_{Iu}	5, 10

$$\boldsymbol{G}_{uu} = \frac{\frac{1}{2C_{eq}s}\begin{bmatrix} D_d^s & D_q^s \end{bmatrix}\boldsymbol{Z}_{RL}^{-1}}{1+\frac{1}{2C_{eq}s}\begin{bmatrix} D_d^s & D_q^s \end{bmatrix}\boldsymbol{Z}_{RL}^{-1}\begin{bmatrix} D_d^s \\ D_q^s \end{bmatrix}}$$

$$\boldsymbol{G}_{ud} = \frac{\frac{1}{2C_{eq}s}(\begin{bmatrix} I_{nd}^s & I_{nq}^s \end{bmatrix} - U_{eq}\begin{bmatrix} D_d^s & D_q^s \end{bmatrix}\boldsymbol{Z}_{RL}^{-1})}{1+\frac{1}{2C_{eq}s}\begin{bmatrix} D_d^s & D_q^s \end{bmatrix}\boldsymbol{Z}_{RL}^{-1}\begin{bmatrix} D_d^s \\ D_q^s \end{bmatrix}}$$

$$\boldsymbol{G}_{id} = -\boldsymbol{Z}_{fp}^{-1}\left(\frac{1}{2C_{eq}s}\begin{bmatrix} D_d^s \\ D_q^s \end{bmatrix}\begin{bmatrix} I_{nd}^s & I_{nq}^s \end{bmatrix} + \begin{bmatrix} U_{eq} & 0 \\ 0 & U_{eq} \end{bmatrix}\right)$$

$$\boldsymbol{Z}_{fp}^{-1} = \left(\boldsymbol{Z}_{RL} + \frac{1}{2C_{eq}s}\begin{bmatrix} D_d^{s2} & D_d^s D_q^s \\ D_d^s D_q^s & D_q^{s2} \end{bmatrix}\right)^{-1}$$

$$\begin{aligned}\boldsymbol{Z}_{re}^{-1} = {} & (\boldsymbol{I}_{2x2} - \boldsymbol{G}_{icd}(\boldsymbol{I}_{2x2} + \boldsymbol{G}_{de}\boldsymbol{G}_{cic}\boldsymbol{G}_{cu}K_u\boldsymbol{G}_{udd})^{-1} \\ & \boldsymbol{G}_{de}(\boldsymbol{G}_{dei} + \boldsymbol{G}_{cic})\cdot\boldsymbol{H}_{idq}\boldsymbol{K}_i)^{-1} \\ & \cdot(\boldsymbol{G}_{icd}(\boldsymbol{I}_{2x2} + \boldsymbol{G}_{de}\boldsymbol{G}_{cic}\boldsymbol{G}_{cu}K_u\boldsymbol{G}_{udd})^{-1} \\ & \boldsymbol{G}_{de}((\boldsymbol{G}_{pll}^d + (\boldsymbol{G}_{dei} + \boldsymbol{G}_{cic})\boldsymbol{G}_{pll}^i + \boldsymbol{G}_{ce}\boldsymbol{G}_{pll}^e)\boldsymbol{H}_{edq}\boldsymbol{K}_e \\ & - \boldsymbol{G}_{cic}\boldsymbol{G}_{cu}K_u\boldsymbol{G}_{ude}) + \boldsymbol{Z}_{in\_ol}^{-1})\end{aligned}$$

where the transfer matrices are discussed in [16].

$$G_{pll} = \frac{k_{Ppll}s + k_{Ipll}}{s^2 + U_{nd}^{s'}k_{Ppll}s + U_{nd}^{s'}k_{Ipll}}$$

$$\begin{aligned}\boldsymbol{A} = {} & \boldsymbol{M}(\boldsymbol{G}_{id}(\boldsymbol{I}_{2x2} + \boldsymbol{G}_{dd}\boldsymbol{G}_{del}\boldsymbol{G}_{ci}\boldsymbol{G}_{dc}k_{dc}\boldsymbol{G}_{ud})^{-1} \\ & \cdot\boldsymbol{G}_{dd}\boldsymbol{G}_{del}\boldsymbol{G}_{ci}(\boldsymbol{k}_{ic}\boldsymbol{Z}_{re}^{-1} - \boldsymbol{G}_{dc}\cdot k_{dc}\boldsymbol{G}_{uu}) + \boldsymbol{Z}_{fp}^{-1})\end{aligned}$$

$$\boldsymbol{B} = \boldsymbol{M}\boldsymbol{G}_{id}(\boldsymbol{I}_{2x2} + \boldsymbol{G}_{dd}\boldsymbol{G}_{del}\boldsymbol{G}_{ci}\boldsymbol{G}_{dc}k_{dc}\boldsymbol{G}_{ud})^{-1}\boldsymbol{G}_{dd}$$

$$\begin{aligned}\boldsymbol{C} = {} & \boldsymbol{G}_{del}\boldsymbol{G}_{ci}(-\boldsymbol{H}_{lf}\boldsymbol{H}_{icdq}\cdot\boldsymbol{k}_{ic}\boldsymbol{Z}_{re}^{-1} \\ & - (\boldsymbol{G}_{pll}^{icc} + \boldsymbol{H}_{lf}\boldsymbol{G}_{pll}^{ic})\boldsymbol{H}_{udq}\boldsymbol{k}_{un})\end{aligned}$$

in which

$$\begin{aligned}\boldsymbol{M} = {} & (\boldsymbol{I}_{2x2} - \boldsymbol{G}_{id}(\boldsymbol{I}_{2x2} + \boldsymbol{G}_{dd}\boldsymbol{G}_{del}\boldsymbol{G}_{ci}\boldsymbol{G}_{dc}k_{dc}\boldsymbol{G}_{ud})^{-1} \\ & \boldsymbol{G}_{dd}\boldsymbol{G}_{del}\boldsymbol{G}_{ci}\boldsymbol{k}_{in})^{-1}.\end{aligned}$$

REFERENCES

[1] Z. Liu, G. Zhang, and Y. Liao, "Stability research of high-speed railway EMUs and traction network cascade system considering impedance matching," *IEEE Trans. Ind. Appl.*, vol. 52, no. 5, pp. 4315–4326, Sep./Oct. 2016.

[2] X. Zhang, J. Chen, R. Qiu, and Z. Liu, "VCT-AOC comprehensive method to suppress high-frequency resonance and low-frequency oscillation in railway traction power supply system," *IEEE Access*, vol. 7, pp. 152202–152213, 2019.

[3] H. Wang, M. Wu, and J. Sun, "Analysis of low-frequency oscillation in electric railways based on small-signal modeling of vehicle-grid system in *dq* frame," *IEEE Trans. Power Electron.*, vol. 30, no. 9, pp. 5318–5330, Sep. 2015.

[4] X. Jiang, H. Hu, X. Yang, Z. He, Q. Qian, and P. Tricoli, "Analysis and adaptive mitigation scheme of low-frequency oscillations in AC railway traction power systems," *IEEE Trans. Transp. Electrific.*, vol. 5, no. 3, pp. 715–726, Sep. 2019.

[5] Z. Liu, Z. Geng, S. Wu, X. Hu, and Z. Zhang, "A passivity-based control of Euler–Lagrange model for suppressing voltage low-frequency oscillation in high-speed railway," *IEEE Trans. Ind. Inf.*, vol. 15, no. 10, pp. 5551–5560, Oct. 2019.

[6] Z. Liu, Y. Wang, S. Liu, Z. Li, H. Zhang, and Z. Zhang, "An approach to suppress low-frequency oscillation by combining extended state observer with model predictive control of EMUs rectifier," *IEEE Trans. Power Electron.*, vol. 34, no. 10, pp. 10282–10297, Oct. 2019.

[7] K. Jiang, C. Zhang, and X. Ge, "Low-frequency oscillation analysis of the train-grid system based on an improved forbidden-region criterion," *IEEE Trans. Ind. Appl.*, vol. 54, no. 5, pp. 5064–5073, Sep./Oct. 2018.

[8] S. Wu, Z. Liu, Z. Li, H. Zhang, and X. Hu, "Impedance modeling and stability analysis in vehicle-grid system with CHB-STATCOM," *IEEE Trans. Power Syst.,* vol. 35, no. 4, pp. 3026–3039, Jul. 2020.

[9] Y. Liao, Z. Liu, G. Zhang, and C. Xiang, "Vehicle-grid system modeling and stability analysis with forbidden region-based criterion," *IEEE Trans. Power Electron.*, vol. 32, no. 5, pp. 3499–3512, May 2017.

[10] L. Wu and W. Ming, "Single-phase cascaded H-bridge multi-level active power filter based on direct current control in ac electric railway application," *IET Power Electron*, vol. 10, no. 6, pp. 637–645, 2017.
[11] L. Harnefors, M. Bongiorno, and S. Lundberg, "Input-admittance calculation and shaping for controlled voltage-source converters," *IEEE Trans. Ind. Electron.*, vol. 54, no. 6, pp. 3323–3334, Dec. 2007.
[12] J. Lyu, X. Cai, and M. Molinas, "Frequency domain stability analysis of MMC-based HVdc for wind farm integration," *IEEE J. Emerg. Sel. Topics Power Electron.,* vol. 4, no. 1, pp. 141–151, Mar. 2016.
[13] B. Wen, R. Burgos, D. Boroyevich, P. Mattavelli, and Z. Shen, "AC stability analysis and *dq* frame impedance specifications in power-electronics-based distributed power systems," *IEEE J. Emerg. Sel. Topics Power Electron.*, vol. 5, no. 4, pp. 1455–1465, Dec. 2017.
[14] H. Zhang, Z. Liu, S. Wu, and Z. Li, "Input impedance modeling and verification of single-phase voltage source converters based on harmonic linearization," *IEEE Trans. Power Electron.*, vol. 34, no. 9, pp. 8544–8554, Sep. 2019.
[15] C. Zhang, M. Molinas, S. Føyen, J. A. Suul, and T. Isobe, "Harmonic-domain SISO equivalent impedance modeling and stability analysis of a single-phase grid-connected VSC," *IEEE Trans. Power Electron.*, vol. 35, no. 9, pp. 9772–9785, Sep. 2020.
[16] Y. Liao, Z. Liu, H. Zhang, and B. Wen, "Low-frequency stability analysis of single-phase system with *dq*-frame impedance approach—Part I: Impedance modeling and verification," *IEEE Trans. Ind. Appl.*, vol. 54, no. 5, pp. 4999–5011, Sep./Oct. 2018.
[17] J. Xu, Q. Qian, B. Zhang, and S. Xie, "Harmonics and stability analysis of single-phase grid-connected inverters in distributed power generation systems considering phase-locked loop impact," *IEEE Trans. Sustain. Energy*, vol. 10, no. 3, pp. 1470–1480, Jul. 2019.
[18] H. Yang *et al.*, "Average-value model of modular multilevel converters considering capacitor voltage," in *Proc. IEEE Appl. Power Electron. Conf. Expo.*, Long Beach, CA, USA, 2016, pp. 1462–1467.
[19] B. Wen, D. Boroyevich, R. Burgos, P. Mattavelli, and Z. Shen, "Analysis of *d-q* small-signal impedance of grid-tied inverters," *IEEE Trans. Power Electron.*, vol. 31, no. 1, pp. 675–687, Jan. 2016.
[20] J. C. Willems, "Dissipative dynamical systems, part I: General theory," *Arch. Ration. Mech. Anal.*, vol. 45, no. 5, pp. 321–351, Jan. 1972.
[21] R. A. Horn and C. R. Johnson, "Hermitian matrices, symmetric matrices, and congruences," in *Matrix Analysis*, 2nd ed. New York, NY, USA, USA: Cambridge Univ. Press, 2013, pp. 225–312.

Siqi Wu (Student Member, IEEE) received the B.S. degree in electrical engineering and automation from Huaqiao University, Xiamen, China, in 2016. She is currently working toward the Ph.D. degree with the School of Electrical Engineering, Southwest Jiaotong University, Chengdu, China.

Her research interests include the control, modeling and stability analysis of power electronics-based systems.

Zhigang Liu (Senior Member, IEEE) received the Ph.D. degree in power system and its automation from Southwest Jiaotong University, Chengdu, China, in 2003.

He is currently a Full Professor with School of Electrical Engineering, Southwest Jiaotong University. His research interests include the electrical relationship of EMUs and traction, detection and assessment of pantograph-catenary in high-speed railway. He has written three books and published more than 200 peer-reviewed journal and conference papers.

Prof. Liu was elected as a fellow of The Institution of Engineering and Technology in 2017. He is an Associate Editor of IEEE TRANSACTIONS ON NEURAL NETWORKS AND LEARNING SYSTEMS, IEEE TRANSACTIONS ON VEHICULAR TECHNOLOGY, IEEE TRANSACTIONS ON INSTRUMENTATION AND MEASUREMENT and IEEE ACCESS. He received the IEEE TIM's Outstanding Associate Editors for 2019 as well as the Outstanding Reviewer of IEEE TRANSACTIONS ON INSTRUMENTATION AND MEASUREMENT 2018.